Results in Physics 24 (2021) 104195

Contents lists available at ScienceDirect

Results in Physics

journal homepage: www.elsevier.com/locate/rinp

On-chip octave-spanning supercontinuum generation in hybrid slot waveguide by power-efficient dual pump

Kangzhu Zhou [a], Qian Li [a,*], Zhe Kang [b,c,*], Jiayao Huang [a], P.K.A. Wai [c]

[a] School of Electronic and Computer Engineering, Peking University, Shenzhen 518055, China
[b] Ningbo Research Institute, Zhejiang University, Ningbo, China
[c] Photonics Research Centre, Department of Electronic and Information Engineering, The Hong Kong Polytechnic University, Hung Hom, Kowloon, Hong Kong

ARTICLE INFO

Keywords:
Supercontinuum
Frequency comb
Integrated optics

ABSTRACT

We propose an on-chip cascaded structure consisting of a microresonator and a slot waveguide to generate the high-performance supercontinuum harnessing the dual pump scenario. Utilizing a single CW pump with the power of only 0.1 W, the dissipative Kerr soliton with the full width at half maximum of 69.2 fs and the peak power of 103.3 W is generated and couples out the microresonator together with the CW pump to serve as a dual pump seed for the supercontinuum generation in the followed slot waveguide. The slot waveguide built upon a silicon-organic hybrid structure is carefully designed to possess remarkable nonlinearity and appropriate dispersion profile for smooth and broadband supercontinuum generation. We have numerically achieved the 1.56 octave-spanning supercontinuum spanning 1 ~ 3 μm with the proposed dual pump scenario. The supercontinuum generated by the dual pump scenario shows flattened, broadband, and quasi-right-angled-trapezoid shape, along with good coherence. Compared with the single pump scenario of CW or soliton pulse only, the supercontinuum generated by the dual pump scenario possesses the much stronger spectrum, broader spanning, and medium coherence. Our work opens up a new path for on-chip and cost-effective supercontinuum generation with the high performance of intensity, bandwidth, and coherence.

Introduction

The inherent characteristic of nonlinear optics is the spectral broadening as well as the new frequency components generation [1]. Supercontinuum (SC) generation known as a representative branch of nonlinear phenomena generates coherent sources with dramatically broadened spectrum using the narrow band seeds [1]. The generation of high-quality SC attracts significant interests in multitudinous research fields, e.g. spectroscopy, metrology, medical imaging, and telecommunications. The numerous applications of SC in these fields include the trace gas sensing [2], velocity and temperature measurements [3], optical coherence tomography (OCT) [4], wavelength division multiplexing [5], etc. The research of SC was pushed to a climax since the experimental demonstration in the photonic crystal fibers in 2000 [6]. In the following two decades, the development of SC generation in optical fibers came a long way [7–10]. At the same time, the frequency comb has attracted increasing attention due to the wide applications in metrology and spectroscopy [11]. However, the inherent small nonlinearity of bulky fiber platforms requires increasing either the pump power or the propagation length to generate the broadband SC, which sets a huge obstacle to the cost-efficiency, miniaturization, and integration.

In recent years, the research hot spot of SC has shifted from the fiber-based platforms to the monolithic waveguide platforms. The nonlinear waveguides built upon Group IV and III-V semiconductors exhibit many advantages, e.g. compactness, extremely tight mode confinement, large nonlinearity, dispersion tailoring capability, and compatibility with the CMOS process [12,13]. Recently, the SC generation in waveguide platforms has been extensively reported. The ultra-broadband SC spanning 470 ~ 2130 nm in the silicon nitride waveguide has been demonstrated [14]. Johnson et al. demonstrated the generation of a SC spanning more than 1.4 octaves in a silicon nitride waveguide by using the sub-100-fs pulses [15]. The experiment of linearly polarized 2 ~ 10 μm SC generation in a chalcogenide rib waveguide has also been achieved [16]. Build upon the previous works on single devices, the combinations of several devices for higher performance SC or frequency comb have been explored. In very recent years, some complex structures containing diverse devices, e.g. the microresonator, highly nonlinear fiber, and

* Corresponding authors.
E-mail addresses: liqian@pkusz.edu.cn (Q. Li), kangtony9999@163.com (Z. Kang).

https://doi.org/10.1016/j.rinp.2021.104195
Received 22 December 2020; Received in revised form 24 February 2021; Accepted 9 April 2021
Available online 16 April 2021

amplifier, have been proposed to generate the SC or frequency comb with the broader spectrum and larger spectral intensity [17,18]. For example, a fully integrated comb generator with a spectral broadening module was investigated by Wang et al. to achieve the high-power comb lines for self-referenced stabilization in 2016 [18]. The spectral broadening module contains many components, e.g. a filter to remove the CW component, an amplifier to enhance the filtered spectrum, and a nonlinear waveguide to further broaden the spectrum. However, the feasibility of the scheme in [18] critically relies on the on-chip amplifiers, which limits the practical application on the non-heterogeneous platforms.

The reported works show that the SC sources with longer pump pulses, e.g. the picosecond, nanosecond, and even CW, are cost-effective and more practical in the diverse applications [19–21]. But, the SCs generated by the CW or quasi-CW pump are typically very noisy and incoherent due to the modulation instability (MI) domination [22]. Thus, it is difficult to generate the coherent and broadband SC in the waveguide with the CW laser, especially under a low power level. Commonly, as an alternative, the SC generated by ultrashort femtosecond pulse seed can obtain a less noisy and highly coherent spectrum [6]. However, the high-power femtosecond laser sources are practically very expensive and require careful handling as well as maintenance, which limits its wide applications out-of-lab. Moreover, the distinct and localized fundamental soliton components ejected from the femtosecond seed make the SC not smooth [22]. It is desirable to possess the advantages of CW and ultrashort pulse sources at the same time to avoid the above-mentioned disadvantages.

In this paper, we propose an on-chip cascaded structure to generate ultrashort dissipative Kerr soliton (DKS) in microresonator first with low power CW pump. Then, the DKS couples with the CW pump to serve as the dual pump for the high-performance SC generation in followed slot waveguide. Typically, joint high nonlinearity and appropriate anomalous dispersion characteristics provide SC generation with high performance. To satisfy these requirements, the slot waveguide is carefully designed to tailor the dispersion and nonlinearity in section 2. In section 3, the performance of the DKS and frequency comb generation inside microresonator is studied. Next, the results of the SC generation in the followed hybrid slot waveguide driven by the dual pump are studied in section 4. In order to highlight the advantages of the SC generated by the dual pump scenario, we carry out a systematic study in section 5 to evaluate the performance of the spectrum, coherence, and signal-to-noise ratio (SNR) under the dual pump, CW pump only, and soliton pump only scenarios. Finally, we draw the conclusions about the performances, superiorities, and potential applications of the SC harnessing the dual pump scenario.

Principle and design

The schematic diagram of SC generation in the proposed on-chip cascaded structure is shown in Fig. 1. The silicon nitride microresonator is followed by the silicon-organic hybrid (SOH) slot waveguide to construct the proposed integrated structure. The 1550 nm CW pump drives the microresonator to generate DKS firstly and then couples with it to seed the followed slot waveguide for SC generation. Deterministic generation of single DKS in microresonator has been confirmed by using either specific pump-resonance scanning or pulse triggering method [23,24]. The simple cascaded structure without any filter and amplifier confirms the great potential to develop a compact, cost-effective, and power-efficient SC generation platform. It is known that high nonlinearity and flattened dispersion profile are beneficial for the broadband and smooth SC, especially under a low pump power condition. Thus, the selection of materials and the design of waveguide geometrics are necessary. The poly (bis p-toluene sulfonate) of 2, 4-hexadiyne-1, 6-diol (PTS) single crystal polymer material, as an attractive optical organic material, has many excellent optical properties, e.g. high nonlinear refractive index and negligible two-photon absorption (TPA) effect [25]. The nonlinear refractive index of PTS is $n_2 = 2.2 \times 10^{-16}$ m^2/W, which is about four orders of magnitude larger than that of the silica (@ $n_2 = 2.48 \times 10^{-20}$ m^2/W) [13]. Compared with the strip waveguide, the slot waveguide can offer a much smaller effective area, thus significantly improving the nonlinearity. Moreover, the scattering loss induced by the sidewall roughness can be minimized by harnessing the horizontal slot structure instead of the vertical slot structure [26,27]. Fig. 2(a) shows the 3D view and cross-section of the proposed SOH slot waveguide. The waveguide has a PTS core layer sandwiched by two silicon cladding layers [25].

The geometrical parameters of the slot waveguide are optimized to obtain the high nonlinear coefficient and appropriate dispersion profiles based on the finite element method. The width and height of the silicon layer are chosen as $W = 260$ nm and $H = 270$ nm, respectively. The calculated group velocity dispersion (GVD) profiles as a function of wavelength are shown in Fig. 2(b) at different heights of the slot. The optimized height of the slot core layer is found to be $S = 30$ nm because the corresponding zero-dispersion wavelength of GVD profile is closer to the pump wavelength (@1550 nm), which is beneficial for broadband and smooth SC generation. As shown by the blue dotted curve in Fig. 2(c), the dispersion profile is also tailored to a flat saddle-shape that can enhance the flatness of SC [28]. Moreover, the inset of Fig. 2(c) shows that most of the electric field is tightly confined inside the narrow slot core, indicating that the proposed waveguide possesses the excellent mode confinement ability. The profile of third-order dispersion (TOD) around 1550 nm in Fig. 2(d) is close to 0, which confirms the flattened GVD profile in Fig. 2(c). According to the definition of $\gamma = 2\pi n_2/(\lambda A_{\mathrm{eff}})$, the nonlinear coefficient γ is inversely proportional to the effective

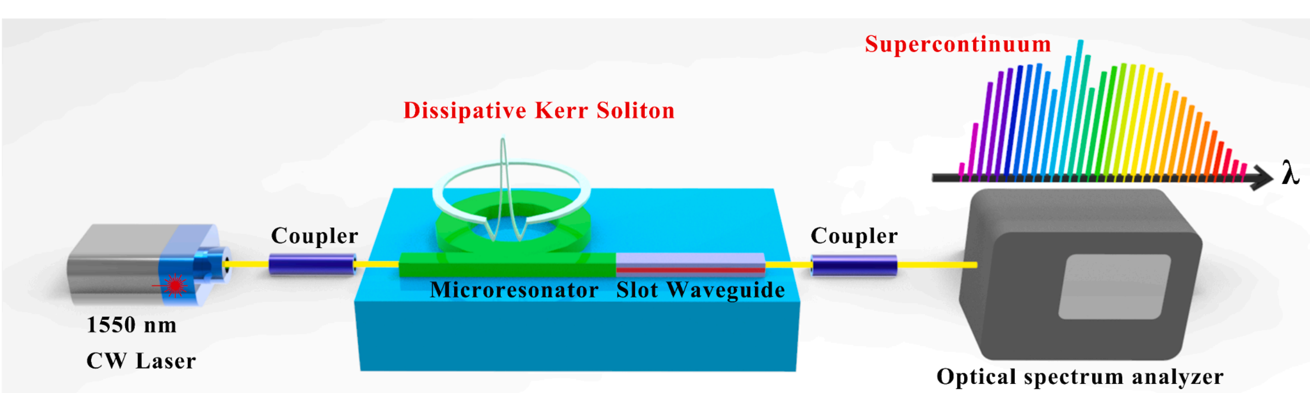

Fig. 1. The schematic diagram of CW laser, couplers, optical spectrum analyzer, and the proposed on-chip cascaded structure consisting of a microresonator and a hybrid slot waveguide for the SC generation harnessing the dual pump scenario.

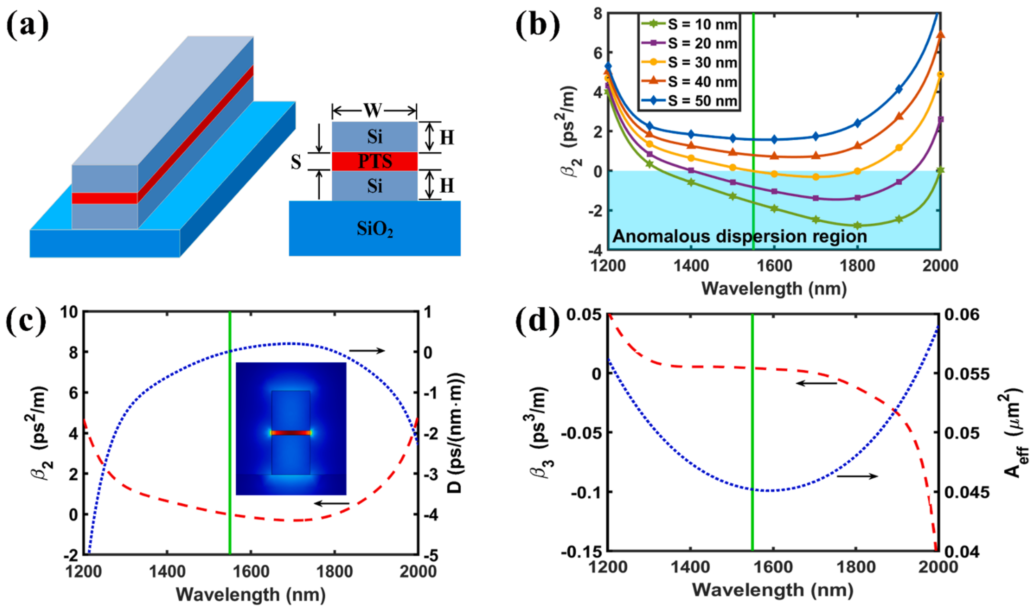

Fig. 2. (a) 3D structure of slot waveguide and its cross-section. (b) GVD profiles with the slot height S increasing from 10 to 50 nm. (c) GVD (red dash curve) as well as the dispersion (blue dotted curve) profiles and the 1550 nm quasi-TM mode polarization (the inset) of the slot waveguide. (d) TOD (red dash curve) and effective area (blue dotted curve) profiles. The curves in (b), (c), and (d) are calculated as the functions of wavelength and the green vertical lines indicate 1550 nm. (For interpretation of the references to colour in this figure legend, the reader is referred to the web version of this article.)

areaA_{eff}. Fig. 2(d) shows the effective area is tailored to be minimum around the 1550 nm pump wavelength. The nonlinear coefficient thus can reach as large as 19731 W^{-1}/m to guarantee efficient nonlinear interaction within a shorter propagation length.

Dual pump generation

In order to generate the dual pump, the DKS is firstly generated in the microresonator driven by a low power (@0.1 W) CW pump. The intracavity dynamic of the CW-driven microresonator is governed by the Ikeda map [29] including the GVD, TOD, and self-phase modulation (SPM) terms, which is given by [30],

$$E^{m+1}(t,0)=\sqrt{\theta}E_{in}+\sqrt{1-\theta}e^{i\varphi_0}E^{m}(t,L),$$

$$\frac{\partial E^{\mathrm{m}}}{\partial z}+\frac{\alpha_{\mathrm{i}}}{\mathbf{2}}E^{\mathrm{m}}+i\frac{\beta_2}{\mathbf{2}}\frac{\partial^2 E^{\mathrm{m}}}{\partial t^2}-\frac{\beta_3}{\mathbf{6}}\frac{\partial^3 E^{\mathrm{m}}}{\partial t^3}=i\gamma|E^{\mathrm{m}}|^2E^{\mathrm{m}},$$

where $E(t,\ z)$, t, z, and L are the slowly varying envelope of the field, the retarded time variable, the propagation step variable, the roundtrip length of the microresonator, respectively. The $E^{\mathrm{m}+1}(t,0)$ is the intracavity field at the beginning of the $m+1$-th roundtrip, which is the coupled result between the driving field E_{in} and the intracavity field at the end of the m-th roundtrip $E^{\mathrm{m}}(t,\ L)$. θ indicates the coupling coefficient between the microring and the bus waveguide of the microresonator. φ_0 is the linear phase shift. α_{i}, β_2, β_3, and γ represent the linear loss, GVD parameter, TOD parameter, and nonlinear coefficient of the microresonator, respectively. The right-hand side of Eq. (2) depicts the SPM process. We define in our simulation the parameters of microresonator as $\beta_2\ =\ -160$ ps^2/km,$\beta_3\ =\ 3.3$ ps^3/km, $\gamma\ =\ 0.9$ W^{-1}/m, $\alpha_{\mathrm{i}}\ = 0.2$ dB/cm [18], $\theta\ = 0.0038$, and $L\ = 0.715$ mm, respectively.

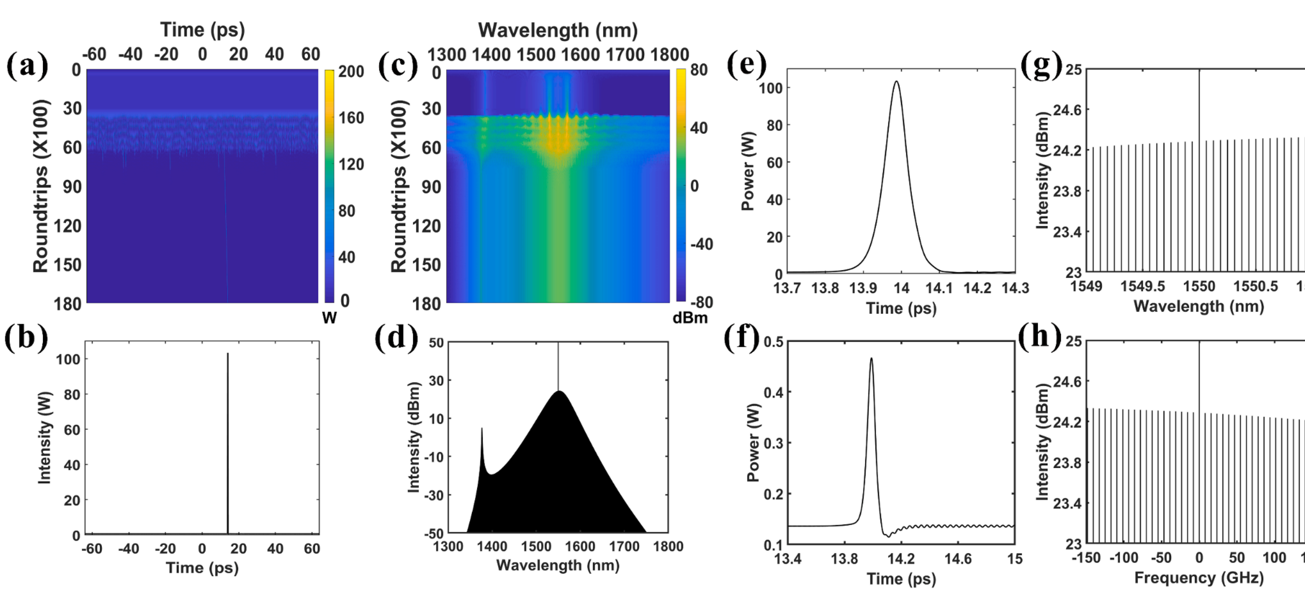

Fig. 3. The (a, c) evolutions of the optical field inside microresonator and (b, d) instantaneous profiles at the final 1,8000 roundtrips as well as their (e, g, h) partially zoom-in part in (a, b, e) time domain and (c, d, g, h) frequency domain. (f) The temporal profile at the through port of microresonator. The comb spectrum is shown with (g) wavelength and (h) frequency scales.

As shown in Fig. 1, we utilize the CW pump with the power of 0.1 W and center wavelength of 1550 nm to drive the microresonator. Fig. 3(a) and 3(b) show the temporal evolution profile inside the microresonator and the instantaneous temporal profile at the final 18,000 roundtrips. We note that DKS is excited before 9000 roundtrips and the roundtrips are extended from 9000 to 18,000 to show the stable state of DKS more clearly. By scanning the pump frequency across the cavity resonance frequency to reach the effective red-detuned condition, the single DKS state is excited at 8,660 roundtrips. We observe in Fig. 3(e) that the peak power and full width at half maximum (FWHM) of the single DKS inside the resonator are 103.3 W and 69.2 fs, respectively. The DKS has a weak CW background with the power of 0.75 W. Fig. 3(c) shows the corresponding spectral evolution inside the microresonator, indicating that a relatively broad spectrum is obtained after the DKS is excited. There is an obvious MI product before 3,000 roundtrips and subsequently the spectrum evolution moves to the stage of cascaded four-wave mixing (FWM) [22]. Fig. 3(d) shows the instantaneous spectral profile of the single DKS at the final 18,000 roundtrips. A frequency comb with a smooth sech^2-shaped profile and bandwidth of 293.3 nm at the –30 dBm level is achieved. The peak on the frequency comb at 1377 nm is induced by the dispersive wave generation due to the perturbation of high-order dispersion [31] and the nonlinear round-trip phase shift [32]. The peak at 1377 nm will disappear if only the GVD parameter is considered. Fig. 3(g) shows the partially zoom-in view of the comb spectrum around the pump wavelength, which has evenly spaced comb lines with the identical wavelength interval of 0.0626 nm. Fig. 3(h) shows the corresponding comb spectrum with frequency scale, indicating clearly the identical frequency interval of 7.81 GHz equal to the free spectral range of the microresonator.

The microresonator used in the simulation has a high Q-factor so that only a small fraction of the CW pump is coupled into the cavity and a small fraction of the intracavity DKS is coupled out. Most of the input CW field will directly propagate through the bus waveguide and coherently couple with the output DKS at the through port of the microresonator. The output field is given by,

$$E_{out} = \sqrt{1-\theta}E_{in} + \sqrt{\theta}E_{cavity}e^{\frac{\pi}{2}i},$$

where E_{out}, E_{in}, and E_{cavity} are the output field of microresonator, the input field of microresonator, i.e. CW pump, and the intracavity field inside the microresonator, respectively. Fig. 3(f) shows the temporal profile of the output field. We observe that a complex-shaped pulse with the peak power of ~0.47 W superimposed on the CW background of ~0.14 W is obtained. The oscillatory tail is induced by the dispersive wave generation [33]. The complex pulse will serve as the dual pump to further generate SC in the followed slot waveguide.

Performance of SC harnessing dual pump

The SC generation in the proposed SOH slot waveguide is governed by nonlinear Schrödinger equation including the three-photon absorption (3PA) effect, as given by [25],

$$\frac{\partial E}{\partial z} + \frac{\alpha_i}{2}E + i\frac{\beta_2}{2}\frac{\partial^2 E}{\partial t^2} - \frac{\beta_3}{6}\frac{\partial^3 E}{\partial t^3} = i\gamma\left(1 + \frac{i}{\omega_0}\frac{\partial}{\partial t}\right)|E|^2 E$$
$$-\frac{\gamma_{3PA}}{3A_{eff}^2}|E|^4 E,$$

where γ_{3PA} is the 3PA coefficient, and ω_0 depicts the center angular frequency, which can be written as $\omega_0 = 2\pi c/\lambda_0$ with the center wavelength λ_0(@ 1550 nm) in the simulation. The self-steepening is also considered in Eq. (4). Since the optical mode is tightly confined inside the PTS core layer of the SOH slot waveguide, the influences of TPA and free carrier absorption (FCA) of the silicon cladding layers are safely neglected. Raman contribution is also safely neglected for the two reasons. First, Raman scattering is negligible for TM mode of horizontal slot structure [34]. Second, Raman scattering is not important in PTS due to its large Raman frequency shift (@28.6 THz) and narrowband (@310 GHz FWHM) Raman-gain spectrum [25,34].

As mentioned above, the output field of microresonator will be the input field of the followed slot waveguide. The connection loss between the microresonator and the slot waveguide is ignored in our work. The low loss strip-to-slot mode converter demonstrated in [35] can be helpful in practice. The GVD parameter, TOD parameter, and nonlinear coefficient of the SOH slot waveguide at 1550 nm are calculated to be -15.5 ps^2/km, 4.203 ps^3/km, and 19731 W^{-1}/m, respectively. The linear loss is set as $\alpha_{\mathrm{i}} = 4.5$ dB/cm [36]. The process of SC generation can be regarded as a noise sensitive process intrinsically, indicating that the fluctuations of input field induced by noise will significantly affect the stability of SC [22]. The one photon per mode model is adopted to simulate the noise field by adding a random phase noise on each numerical grid point in the frequency domain [37], as given by,

$$\widetilde{E}_{\mathrm{noise}} = \eta\sqrt{P_0}exp\left(i2\pi\widehat{U}\right)$$

where η represents the noise level and P_0 is the peak power of pump field. The $\widehat{U}$ indicates a uniformly distributed random variable between 0 and 1. η is assumed to be 10^{-6} without the special instructions.

The input and output instantaneous spectral profiles and the spectral evolution are shown in Fig. 4. Fig. 4(a) shows the envelope of the spectrum of the input field is very similar to that of the frequency comb in Fig. 3(d), but a lower spectral power on the soliton component. Fig. 4(b) shows the spectrum already undergoes a significant broadening within a short distance of 5 mm due to the large nonlinearity of the SOH waveguide. By setting the center wavelength (@1550 nm) as the boundary, the spectral broadening of the shorter wavelength side is significantly weaker than that of the longer wavelength side because the soliton fission induced red-shifted components is stronger than the blue-shifted one. In addition, we see that there are some small depressions on the spectrum around 1550 nm from 0 to 10 mm propagation. This indicates that the spectrum around 1550 nm is weaker than the other bands, which dramatically affects the flatness of SC. Subsequently, the spectral power around the center wavelength (@1300 ~ 2000 nm) gradually increases to make the SC more flattened. We find the final spectrum shown in Fig. 4(c) changes to a flattened, broadband, and quasi-right-angled-trapezoid shape from an original sharp, narrow, and quasi-triangle shape in Fig. 4(a). Fig. 4(d) shows that soliton fission occurs within 1 mm and the fundamental soliton shifts towards the pulse trailing edge rapidly for the 2 to 5 mm propagation because the group velocity of the red-shifted spectrum of the soliton decreases, which confirms the phenomenon that the spanning of longer wavelength spectrum is broader than that of shorter wavelength spectrum. The obtained bandwidths at –30 dBm level without and with 3PA as the function of propagation length are shown in Fig. 4(e). We note that the propagation length is extended from 25 to 45 mm to make the variation trend clearer. It is clearly seen that the bandwidths at –30 dBm level of the two cases both always decrease as the propagation length increases, especially for the 25 to 30 mm propagation. The bandwidth with 3PA is narrower than that without 3PA during the entire propagation. However, the difference of bandwidth ranges only from 25 to 35 nm, which has a slight influence on the whole spectrum that spanning ~ 2000 nm. The weak effect of 3PA on the spectrum benefits from the low pump power level used.

Evaluation and discussion

We separate the CW and soliton components of the output field at the through port of microresonator and inject them individually into the SOH slot waveguide to highlight the superiorities of the proposed dual pump scenario. Fig. 5 shows that the spectral characteristics of three pump scenarios at different propagation lengths. The instantaneous

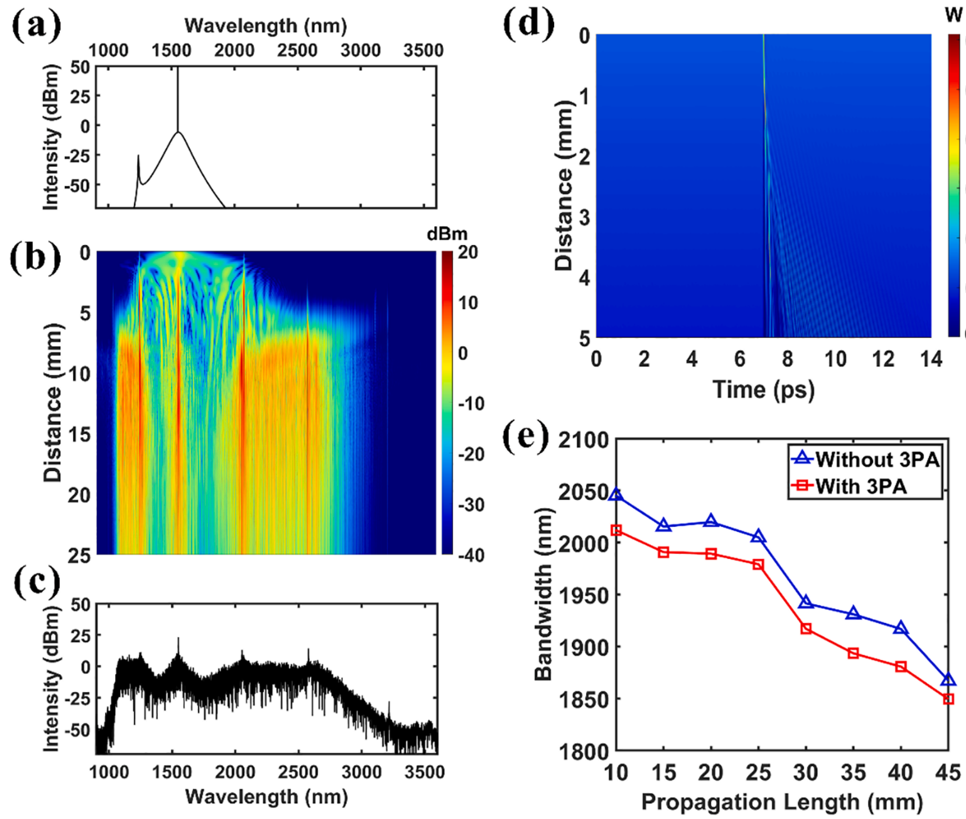

Fig. 4. The (a) input profile, (b) evolution, and (c) output profile of the spectrum with 3PA. (d) Temporal evolution with 3PA from 0 to 5 mm. (e) Bandwidths at –30 dBm level of SC generation in the SOH slot waveguide under different propagation lengths without and with 3PA.

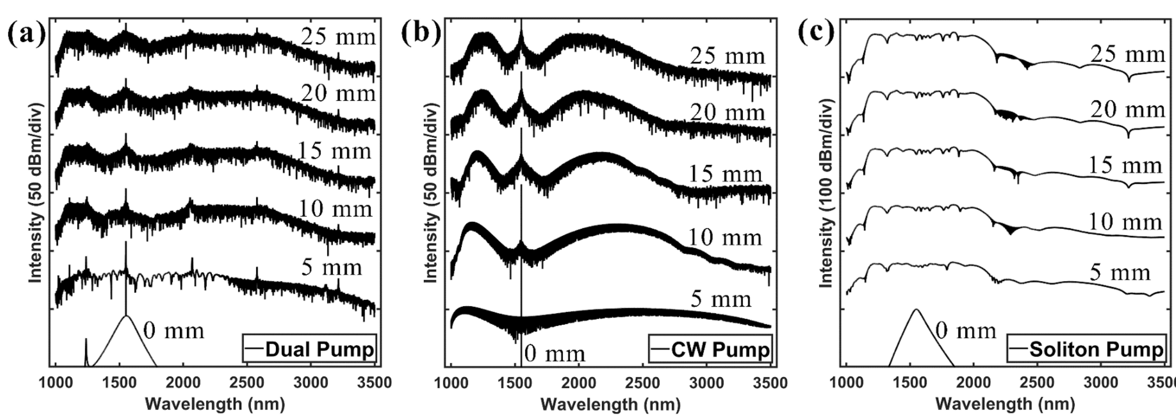

Fig. 5. The instantaneous spectral profiles of (a) dual pump, (b) CW pump only, and (c) soliton pump only scenarios under different propagation lengths.

spectral profiles of different pump scenarios, all undergo a significant spectral broadening during the initial stage of the evolution from 0 to 5 mm because of the large nonlinearity provided by the SOH slot waveguide. The two MI sidelobes gradually appear in the spectrum of CW pump only scenario in Fig. 5(b), which depicts that the power of the MI sidelobes grows larger and faster than the spectrum around 1550 nm. Fig. 5(c) shows the instantaneous profile of the soliton pump only scenario becomes a quasi-rectangular shape from an original triangle shape from 0 to 10 mm propagation. We can observe that the spectral shape is almost maintained from 10 to 25 mm propagation. As shown in Fig. 5(b), the MI effect which is a noise-driven process, plays an important role in the CW pumped SC generation [22]. The MI effect amplifies the background noise thus yields the low coherence and poor SNR, as shown in Fig. 6(e) and 6(h). The soliton pumped SC in Fig. 5(c) is dominated by the soliton fission effect rather than the MI effect [22], which brings the much higher coherence and SNR, as shown in Fig. 6(f) and 6(i). Fig. 5(a) shows the dual pumped SC also has background noise due to the contribution of the CW component, but possesses better coherence and SNR (Fig. 6(d) and 6(g)) due to the contribution of the soliton component. Moreover, Fig. 5(a) shows that the dual pumped SC evolves more rapidly compared with that in Fig. 5(b), and reaches the maximal bandwidth in a shorter distance because of the contribution of the soliton component [1]. As mentioned above, the background noise can be suppressed by increasing the proportion of the soliton component in the dual pump by adjusting the power of the input CW driving field.

To avoid the accidental conclusion using the single result, we do 112 individual simulations and calculate their average spectra of different pump scenarios in Fig. 6. Fig. 6(a) shows that the spectrum of dual pump scenario is broadened remarkably compared with the input one after 25 mm propagation. The bandwidths at –20 and –30 dBm levels are 1836

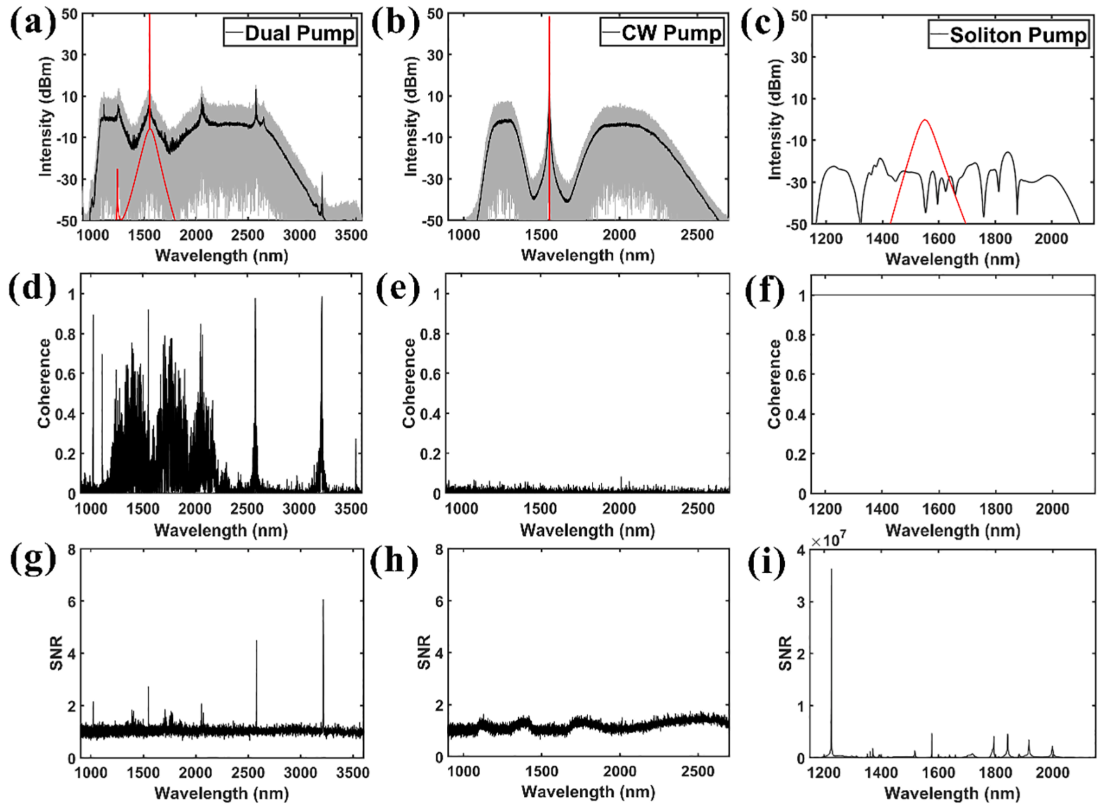

Fig. 6. The (a, b, c) SC, (d, e, f) coherence, and (g, h, i) SNR of (a, d, g) dual pump, (b, e, h) CW pump only, and (c, f, i) soliton pump only scenarios. The red, grey and black curves in (a), (b), and (c) indicate the input fields, the spectra of 112 individual simulations, and their average spectra. (For interpretation of the references to colour in this figure legend, the reader is referred to the web version of this article.)

nm (@1044 ~ 2880 nm) and 1980 nm (@1020 ~ 3000 nm), which reach 1.46 and 1.56 octave-spanning, respectively. Fig. 6(b) shows the spectrum is broadened to some extent with two evident MI sidelobes when the slot waveguide is pumped by the CW pump only. Fig. 6(c) shows that the spectrum generated by the soliton pump only scenario is much narrower and weaker than that of the other two pump scenarios. We conclude from these results that the dual pump scenario generates the much broader and stronger spectrum.

Furthermore, the degree of coherence and the SNR are also calculated and shown in Fig. 6 according to the references [36–38] to compare dual pump scenario with the other two pump scenarios in a more comprehensive and systematic perspective. It is noted that the coherence and SNR of the center wavelength are ignored to avoid interference from the remaining pump component. The degree of coherence is introduced to characterize the noise sensitivity of output spectrum and estimate the coherence of individual simulations. Fig. 6(d) shows the coherence of dual pump has a good performance from 1200 to 2200 nm. The coherence of the CW pump only scenario is almost to 0 for the whole spectrum in Fig. 6(e). Fig. 6(f) shows the coherence of soliton pump only scenario reaches unit over the entire spectral bands because the FWHM of the soliton pulse is as short as 69.2 fs. Thus, soliton fission dominates the SC generation process instead of the MI to achieve excellent coherence. It is apparent that the performance of coherence of the dual pump scenario is between that of the CW and soliton pump only scenarios. Fig. 6(g) shows the multiple SNR peaks of dual pump scenario are larger than 2. In comparison, Fig. 6(h) shows the SNR of CW pump only scenario is very weak and lower than 2. Fig. 6(i) shows that the multiple SNR peaks of soliton pump only scenario are above 10^2 and even up to 10^7, indicating that the noise is much smaller than the output signal. The SNR performance of dual pump scenario is far weaker than that of the soliton pump only scenario but stronger than that of the CW pump only scenario.

As shown in Fig. 7, the overall spectral coherence R and overall SNR are calculated for the spectra at different noise levels to compare the performance of SC among three pump scenarios in a quantitative way [38–40]. Overall spectral coherence R is a single value that can characterize the coherence of overall spectra. Fig. 7(a) shows that the overall spectral coherence of soliton pump only scenario maintains unit when $\log_{10}(\eta)$ increases from –6 to –3, indicating that the spectrum is completely coherent with the noise level below 10^{-3}. As $\log_{10}(\eta)$ increases from –3 to –1, the overall spectral coherence degrades quickly from 1 to 0.15. The degradation is slowed down as $\log_{10}(\eta)$ is close to 0. The overall spectral coherence of the dual pump scenario shares the same trend as that of the soliton pump only scenario. When the noise level is below 10^{-8}, the spectrum of dual pump scenario is completely coherent, i.e. the overall spectral coherence maintains unit. Moreover, the overall spectral coherence of dual pump scenario has a rapid degradation from 1 to 0.13 when $\log_{10}(\eta)$ increases from –8 to –6, indicating that much better coherence can be achieved by controlling the noise level below 10^{-6}. The overall coherence of CW pump only scenario is always close to 0 as $\log_{10}(\eta)$ increases from –9 to –3, indicating the spectrum is extremely noisy even under lower noise level. These results reflect that the noise sensitivity of dual pump scenario is between that of CW and soliton only pump scenarios.

Similarly, the overall SNR can be calculated in a single value to estimate the SNR of whole spectrum [39]. Fig. 7(b) shows that the overall SNR varies with different noise levels in logarithmic scale. As $\log_{10}(\eta)$ increases from –6 to –1, the overall SNR of soliton pump only scenario decreases dramatically from 5×10^5 to 3.2. Besides, we can observe that $log_{10}(\langle \mathrm{SNR} \rangle)$ decreases linearly when $\log_{10}(\eta)$ increases from –6 to –1. The overall SNR will decrease 10 times when the noise level increases 10 times. Similarly, $log_{10}(\langle \mathrm{SNR} \rangle)$ of dual pump scenario shows a linearly decreasing trend that the overall SNR decreases from 200 to 2.4 as $\log_{10}(\eta)$ increases from –9 to –7. The overall SNR of CW pump only

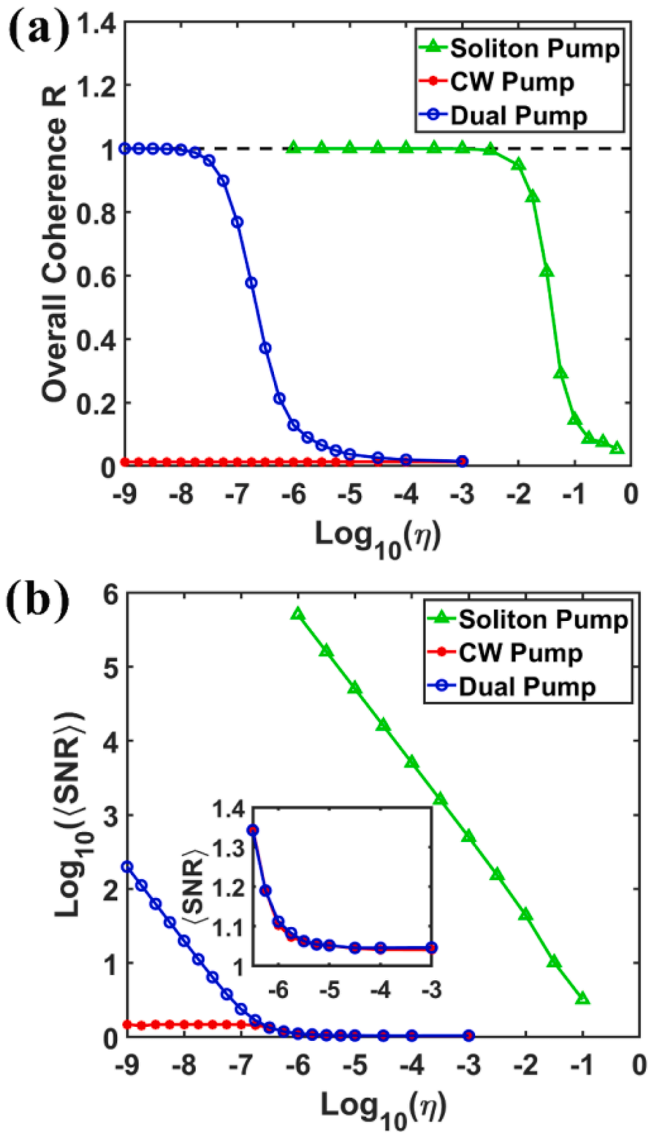

Fig. 7. (a) Overall spectral coherence in linear scale and (b) overall SNR in logarithmic scale of dual pump, CW pump only, and soliton pump only scenarios under different noise levels. The dashed line in (a) represents $R = 1$ and the inset in (b) shows the local part of the overall SNR in linear scale with noise level increasing from $10^{-6.5}$ to 10^{-3}.

scenario maintains 1.5 when $\log_{10}(\eta)$ increases from –9 to –7. The inset of Fig. 7(b) shows the overall SNR of dual pump and CW pump only scenario in linear scale. We can observe that the overall SNR of dual pump scenario is almost same as that of CW pump only scenario when the noise level is above $10^{-6.5}$, indicating the noise tolerance between them is very close. When $\log_{10}(\eta)$ increases from –6.5 to –3, their overall SNR deceases from 1.35 to 1.05. In conclusion, the dual pump scenario shows medium overall spectral coherence and overall SNR under different noise levels, which is between that of the CW and soliton pump only scenarios. The CW pump only scenario shows the weakest coherence and SNR. Although soliton pump only scenario shows the best coherence and SNR, its spectrum is much narrower and weaker than that of dual pump scenario.

Furthermore, Fig. 8 shows that R and $log_{10}(\langle \mathrm{SNR} \rangle)$ are calculated to investigate the evolution trend of overall spectral coherence and overall SNR of the three pump scenarios. It is clear that R and $log_{10}(\langle \mathrm{SNR} \rangle)$ of the soliton or CW pump only scenario exhibit excellent stability during the entire propagation process. Fig. 8(a) shows that the R of soliton pump only scenario is always close to unit while that of CW pump only scenario is always close to 0. The R of dual pump scenario degrades dramatically from 1 to 0.2 when propagating from 5 to 15 mm and no longer decreases after 20 mm. It maintains ~ 0.13 for the 20 to 45 mm propagation. Similarly, Fig. 8(b) shows that $log_{10}(\langle \mathrm{SNR} \rangle)$ of the soliton pump only scenario is always close to 6 while that of the CW pump only scenario is always close to 0 and maintains $\sim$ 0.04. However, $log_{10}(\langle \mathrm{SNR} \rangle)$ of dual pump scenario decreases from 3.3 to 0.05 for the 5 to 20 mm propagation and subsequently maintains $\sim$0.05. The results also confirm that the performance of dual pump scenario on overall spectral coherence and overall SNR is better than that of CW pump only scenario and weaker than that of soliton pump only scenario among the whole propagation. Compared with the traditional single pump scenario of CW or soliton pulse only, the results from Fig. 5–8 show that dual pumped SC possesses the much stronger spectrum, broader spanning, as well as the medium coherence and SNR. The octave-spanning spectrum with better coherence and SNR generated by our method can fulfill the requirements of some applications such as the OCT in biomedical imaging [4] and frequency metrology [15].

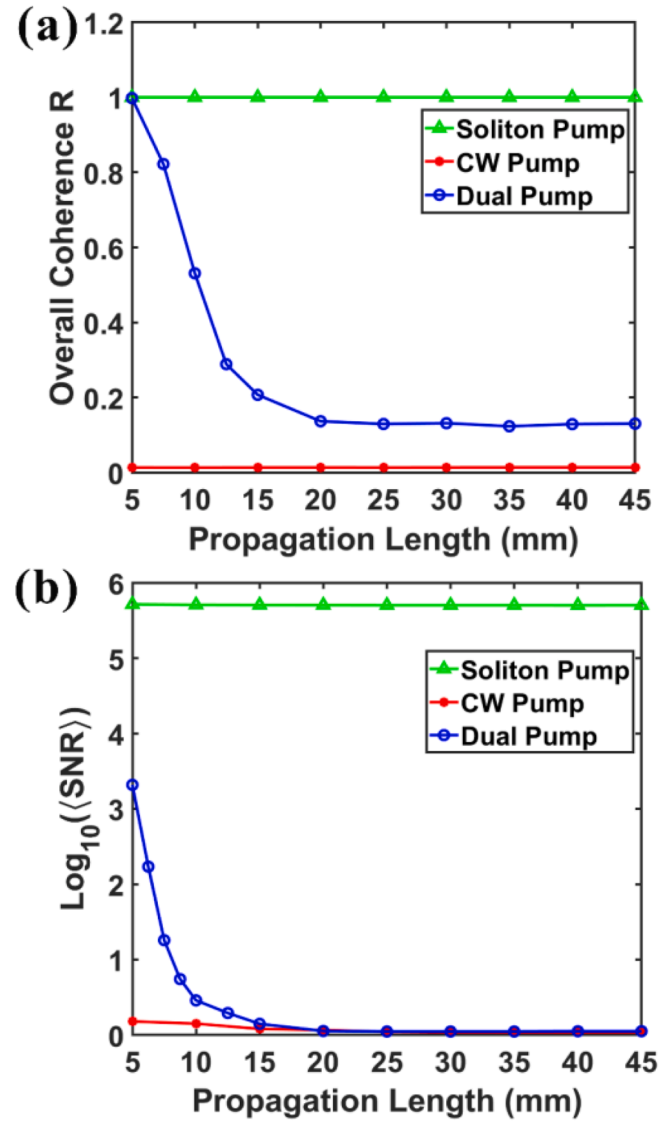

Fig. 8. (a) Overall spectral coherence R in linear scale and (b) overall SNR in logarithmic scale of dual pump, CW pump only, and soliton pump only scenarios under different propagation lengths.

Conclusions

In summary, we propose a simple on-chip structure that a micro-resonator is cascaded by a SOH slot waveguide to achieve the octave-spanning SC with strong intensity and good coherence. The SOH waveguide adopts the horizontal slot structure filled by PTS material with ultrahigh nonlinear refractive index. We carefully design the waveguide to achieve the high nonlinearity as well as the appropriate dispersion profile for the broadband and flattened SC. With a low power (@0.1 W) CW pump only, the dual pump seed which is obtained through the DKS generation in the microresonator, further drives the SOH waveguide and achieves a flattened, quasi-right-angled-trapezoid-shaped, and 1.56 octave-spanning (@1 ~ 3 μm) SC with good coherence. The performances of SC under different pump conditions, i.e. dual pump, CW pump only, and soliton pump only, are comprehensively studied. The coherence and SNR are also evaluated quantitatively. The results show that the bandwidth and spectral intensity of SC by the dual pump scenario is much broader and stronger than that of CW and soliton pump only scenarios. The coherence and SNR of dual pump also have good performance under different noise levels and propagation lengths. Considering the spectrum spanning, intensity, coherence, and SNR for the power-efficient SC generation, the proposed dual pump scenario shows apparent superiority. The results of this work offer a feasible scheme and credible evidence that dual pump scenario is promising for on-chip and high-performance SC generation. The performance is significantly improved by dual pump scenario compared with that of direct-CW-pumping waveguide schemes reported so far, especially under a low pump power. The high-performance SC generation using the proposed power-efficient dual pump method will prospectively find significant and practical applications in high demanding spectroscopy, metrology, and communications.

Funding

This work was supported by the National Natural Science Foundation of China (Project 61675008, 62075188), Shenzhen Science and Technology Innovation Commission (Project GJHZ20180411185015272), Youth Science and Technology Innovation Talent of Guangdong Province (2019TQ05X227).

CRediT authorship contribution statement

Kangzhu Zhou: Methodology, Investigation, Visualization, Writing - original draft. **Qian Li:** Supervision, Methodology, Writing - review & editing. **Zhe Kang:** upervision, Methodology, Writing - review & editing. **Jiayao Huang:** Software, Validation. **P.K.A. Wai:** Conceptualization, Writing - review & editing.

Declaration of Competing Interest

The authors declare that they have no known competing financial interests or personal relationships that could have appeared to influence the work reported in this paper.

References

[1] Dudley JM, Genty G, Coen S. Supercontinuum generation in photonic crystal fiber. Rev Mod Phys 2006;78:1135–84.
[2] Jahromi KE, Pan Q, Høgstedt L, Friis SMM, Khodabakhsh A, Moselund PM, et al. Mid-infrared supercontinuum-based upconversion detection for trace gas sensing. Opt Express 2019;27:24469–80.
[3] König J, Moller S, Granzow N, Cierpka C. On the application of a supercontinuum white light laser for simultaneous measurements of temperature and velocity fields using thermochromic liquid crystals. Exp Therm Fluid Sci 2019;109:109914.
[4] Marks DL, Oldenburg AL, Reynolds JJ, Boppart SA. Study of an ultrahigh-numerical-aperture fiber continuum generation source for optical coherence tomography. Opt Lett 2002;27:2010.
[5] Saghaei H. Supercontinuum source for dense wavelength division multiplexing in square photonic crystal fiber via fluidic infiltration approach. Opt Commun 2017;26:16–22.
[6] Ranka JK, Windeler RS, Stentz AJ. Visible continuum generation in air–silica microstructure optical fibers with anomalous dispersion at 800 nm. Opt Lett 2000;25:25.
[7] Dudley JM, Provino L, Grossard N, Maillotte H, Windeler RS, Eggleton BJ, et al. Supercontinuum generation in air–silica microstructured fibers with nanosecond and femtosecond pulse pumping. J Opt Soc Am B 2002;19:765.
[8] Xia C, Kumar M, Kulkarni OP, Islam MN, Terry Jr FL, Freeman MJ, et al. Mid-infrared supercontinuum generation to 45 μm in ZBLAN fluoride fibers by nanosecond diode pumping. Opt Lett 2006;31:2553.
[9] Kobtsev SM, Smirnov SV. Modelling of high-power supercontinuum generation in highly nonlinear, dispersion shifted fibers at CW pump. Opt Express 2005;13:6912.
[10] Li X, Chen W, Xue T, Gao J, Gao W, Hu L, et al. Low threshold mid-infrared supercontinuum generation in short fluoride-chalcogenide multimaterial fibers. Opt Express 2014;22:24179.
[11] Pasquazi A, Peccianti M, Razzari L, Moss DJ, Coen S, Erkintalo M, et al. Micro-combs: A novel generation of optical sources. Phys Rep 2018;729:1–81.
[12] Leuthold J, Koos C, Freude W. Nonlinear silicon photonics. Nat Photonics 2010;4:535–44.
[13] Koos C, Jacome L, Poulton C, Leuthold J, Freude W. Nonlinear silicon-on-insulator waveguides for all-optical signal processing. Opt Express 2007;15:5976.
[14] Epping JP, Hellwig T, Hoekman M, Mateman R, Leinse A, Heideman RG, et al. On-chip visible-to-infrared supercontinuum generation with more than 495 THz spectral bandwidth. Opt Express 2015;23:19596.
[15] Johnson AR, Mayer AS, Klenner A, Luke K, Lamb ES, Lamont MRE, et al. Octave-spanning coherent supercontinuum generation in a silicon nitride waveguide. Opt Lett 2015;40:5117–20.
[16] Yu Y, Gai X, Ma P, Vu K, Yang Z, Wang R, et al. Experimental demonstration of linearly polarized 2–10 μm supercontinuum generation in a chalcogenide rib waveguide. Opt Lett 2016;41:958.
[17] Lamb ES, Carlson DR, Hickstein DD, Stone JR, Diddams SA, Papp SB. Optical-frequency measurements with a kerr microcomb and photonic-chip supercontinuum. Phys Rev Appl 2018;9:24030.
[18] Wang J, Guo Y, Liu H, Li G, Zhang L. A comparative analysis on fully integrated spectral broadening of kerr frequency combs. IEEE Photon J 2017;9.
[19] Rulkov AB, Vyatkin MY, Popov SV, Taylor JR, Gapontsev VP. High brightness picosecond all-fiber generation in 525–1800nm range with picosecond Yb pumping. Opt Express 2005;13:377.
[20] Kano H, Hamaguchi HO. Dispersion-compensated supercontinuum generation for ultrabroadband multiplex coherent anti-Stokes Raman scattering spectroscopy. J Raman Spectrosc 2006;37:411–5.
[21] Maus M, Rousseau E, Cotlet M, Schweitzer G, Hofkens J, Van Der Auweraer M, et al. New picosecond laser system for easy tunability over the whole ultraviolet/visible/near infrared wavelength range based on flexible harmonic generation and optical parametric oscillation. Rev Sci Instrum 2001;72:36–40.
[22] Li F, Yuan J, Kang Z, Li Q, Wai PKA. Modeling frequency comb sources. Nanophotonics 2016;5:292–315.
[23] Herr T, Brasch V, Jost JD, Wang CY, Kondratiev NM, Gorodetsky ML, et al. Temporal solitons in optical microresonators. Nat Photonics 2014;8:145–52.
[24] Kang Z, Li F, Yuan J, Nakkeeran K, Nathan Kutz J, Wu Q, et al. Deterministic generation of single soliton Kerr frequency comb in microresonators by a single shot pulsed trigger. Opt Express 2018;26:18563–77.
[25] Kang Z, Yuan J, Zhang X, Sang X, Wang K, Wu Q, et al. On-chip integratable all-optical quantizer using strong cross-phase modulation in a silicon-organic hybrid slot waveguide. Sci Rep 2016;6:1–12.
[26] R. Hainberger and P. Muellner, "Nonlinearity of optimized horizontal slot waveguides," 2009 IEEE/LEOS Winter Topicals Meeting Series, Innsbruck, Austria, 2009; 34-35.
[27] Martínez A, Blasco J, Sanchis P, Galán JV, García-Rupérez J, Jordana E, et al. Ultrafast all-optical switching in a silicon-nanocrystal-based silicon slot waveguide at telecom wavelengths. Nano Lett 2010;10:1506–11.
[28] Zhang L, Lin Q, Yue Y, Yan Y, Beausoleil RG, Agarwal A, et al. On-chip octave-spanning supercontinuum in nanostructured silicon waveguides using ultralow pulse energy. IEEE J Sel Top Quantum Electron 2012;18:1799–806.
[29] Coen S, Randle HG, Sylvestre T, Erkintalo M. Modeling of octave-spanning Kerr frequency combs using a generalized mean-field Lugiato-Lefever model. Opt Lett 2013;38:37.
[30] Hansson T, Wabnitz S. Frequency comb generation beyond the Lugiato-Lefever equation: multi-stability and super cavity solitons. J Opt Soc Am B 2015;32:1259.
[31] Bao C, Taheri H, Zhang L, Matsko A, Yan Y, Liao P, et al. High-order dispersion in Kerr comb oscillators. J Opt Soc Am B 2017;34:715.
[32] Jang JK, Erkintalo M, Murdoch SG, et al. Observation of dispersive wave emission by temporal cavity solitons. Opt Lett 2014;39:5503–6.
[33] Kippenberg TJ, Gaeta AL, Lipson M, Gorodetsky ML. Dissipative Kerr solitons in optical microresonators. Science (80-) 2018;361.
[34] Lin Q, Painter OJ, Agrawal GP. Nonlinear optical phenomena in silicon waveguides: modeling and applications. Opt Express 2007;15:16604.
[35] Palmer R, Alloatti L, Korn D, Heni W, Schindler PC, Bolten J, et al. Low-loss silicon strip-to-slot mode converters. IEEE Photonics J 2013;5:2200409.
[36] Polyakov S, Yoshino F, Liu M, Stegeman G. Nonlinear refraction and multiphoton absorption in polydiacetylenes from 1200 to 2200 nm. Phys Rev B 2004;69:1–11.
[37] Dudley JM, Genty G, Eggleton B. Harnessing and control of optical rogue waves in supercontinuum generation. Opt Express 2008;6:3644–51.

[38] Sørensen ST, Larsen C, Møller U, Moselund PM, Thomsen CL, Bang O. Influence of pump power and modulation instabilitygain spectrum on seeded supercontinuumand rogue wave generation. J Opt Soc Am B 2012;29:2875.

[39] Sørensen ST, Larsen C, Møller U, Moselund PM, Thomsen CL, Bang O. The role of phase coherence in seeded supercontinuum generation. Opt Express 2012;20:22886.

[40] Dudley JM, Coen S. Coherence properties of supercontinuum spectra generated in photonic crystal and tapered optical fibers. Opt Lett 2002;27:1180–2.